Energy Storage Materials 90 (2026) 105392

Contents lists available at ScienceDirect

Energy Storage Materials

journal homepage: www.elsevier.com/locate/ensm

The Electrical Double Layer and Autocatalytic NaF formation in Sodium Ion Batteries

Kie Hankins [a,‡], Miftahussurur Hamidi Putra [b,‡], Axel Gross [b], Ulrike Krewer [a,*]

[a] Dr. K. Hankins, Prof. U. Krewer, Institute of Applied Materials – Electrochemical Technologies, Karlsruhe Institute of Technology, Adenauerring 20b, 76131 Karlsruhe, Germany

[b] Dr. M. H. Putra, Prof. Dr. A. Groß, Institute for Theoretical Chemistry, Ulm University, Mez-Starck-Haus, Oberberghof 7, 89081 Ulm, Germany

ARTICLE INFO

Keywords:
Electrochemistry
Solid Electrolyte Interphase
Kinetic Monte Carlo
Density Functional Calculations
Formation

ABSTRACT

The solid electrolyte interphase (SEI) in sodium ion batteries is known to have significant concentrations of NaF, which provides excellent electrochemical stability to the cell. However, the formation mechanism of NaF is unclear. Similarly, the electrical double layer (EDL) is known to have a substantial impact on all electrochemical interfacial processes, but is challenging to model. We employ first principles calculations and kinetic Monte Carlo (kMC) modeling to determine the complex electrochemical phenomena behind the formation of NaF and elucidate the role of the EDL in SEI growth. Novel reaction mechanisms and kinetic parameters for $NaPF_6$ decomposition are determined, where hydrolysis is shown to be unfavorable and a NaF-self catalyzed mechanism is the dominant pathway. KMC simulations reveal the formation of SEIs consisting of an inner layer of Na_2CO_3 and an outer layer of NaF. Higher concentrations of the conductive salt $NaPF_6$ lead to the formation of thinner SEIs with high fractions of NaF. Higher charging rates also generate thinner SEIs, but with higher porosity. An initial molecular-scale model of the EDL and its potential gradient is developed and integrated into the kMC framework, enabling unique insights into the role of the EDL in SEI formation and elucidating its complex relationship with salt concentration and charging rate.

1. Introduction

Sodium-ion batteries (SIBs) have emerged as a promising alternative to lithium ion batteries, offering a potentially more sustainable and cost-effective approach to energy storage [1,2]. SIBs typically exhibit lower energy densities than lithium ion systems, but are still powerful enough to be effective for electric vehicles and grid-scale storage [3]. The primary advantage of SIBs lies in the abundance and widespread availability of sodium, which alleviates concerns related to resource scarcity and supply chain instability. Furthermore, sodium-based battery chemistries are compatible with aluminum current collectors and have the potential to reduce future manufacturing costs and improve the environmental footprint of energy storage technologies [4–6]. Recent advancements in SIB research have accelerated their commercialization, marking a significant step toward their practical implementation [7]. However, several technical challenges must still be addressed to enable the large-scale deployment of SIB technology.

One of the primary challenges faced by SIBs is poor cycle-life stability, largely due to the instability of the solid electrolyte interphase (SEI) [8,9]. The SEI is a protective film that forms from the decomposition of the electrolyte on the anode surface, mainly during the first charge, and ideally functions as a stable barrier that facilitates ion transport while preventing electron leakage and further electrolyte breakdown [10,11]. Excessive growth of the SEI is one of the largest sources of capacity loss in many modern batteries. A stable and effective SEI is vital for battery performance and durability; however, its growth behavior and physicochemical properties remain poorly understood because they are influenced by a complex array of nanoscale phenomena.

Many prior experimental works have investigated the structure and composition of the SEI in SIBs, and have reported heterogeneous, and polycrystalline [12,13] morphologies, with formation mechanisms including both layer-by-layer and cluster growth modes [14–16]. Other works have observed a significantly inorganic inner SEI, composed primarily of Na_2CO_3 and NaF in varied ratios, and an outer layer containing organic sodium salts [17–20].

* Corresponding author.
E-mail address: Ulrike.Krewer@KIT.edu (U. Krewer).
‡ These authors contributed equally to the work.

https://doi.org/10.1016/j.ensm.2026.105392
Received 21 May 2026; Received in revised form 6 July 2026; Accepted 13 July 2026
Available online 14 July 2026

Studies have shown that the SEI components in SIBs exhibit relatively high solubility, indicating that dissolution is likely to be a major driving force of SEI degradation [21,22]. Additionally, Na_2CO_3, one of the primary SEI components, is known to be significantly electron leaking [23,24]. This increased electronic conductivity causes the SEI to be less effective at blocking reactions, leading to greater consumption of the active material and excessive growth of the layer. NaF, another major SEI component, has been shown to be more electronically insulating than Na_2CO_3. The effect of this increased electrical resistivity is visible in the improved performance of cells containing SEIs with high-NaF content compared to cells with a lower presence of NaF [18]. This implies that maximizing the NaF content in the SEI is necessary for effective cells. However, the mechanisms of NaF formation are not yet well understood and may involve other species, such as water contamination [25,26]. Further study is needed in order to elucidate the underlying reaction mechanisms in order to guide the design of robust SEIs.

The electrolyte salt concentration and cell charging rate are known to have a substantial effect on SEI composition and cell performance. Studies have shown that low concentrations of $NaPF_6$ are effective only at low C-rates, and high concentrations are effective at medium C-rates, but begin to cause diminished capacity at high C-rates [27]. The underlying mechanisms of this behavior are complex, as they involve the material properties of the SEI, the reactivity of the electrolyte species towards SEI formation, and the ionic transport behavior of the electrolyte. Similarly, different solvent compositions have been shown to influence SEI behavior, but the exact mechanisms are unclear. This could be due to an electrochemical mechanism, such as reactivity or modification of the electrical double layer (EDL) via altered dielectric constant, or physical in nature, relating to ion solvation and intercalation [28–30]. Salt concentration, C-rate, and solvent composition can also substantially impact the distribution of the EDL, which is known to have a significant effect on all interfacial electrochemical processes, including SEI formation and ion intercalation behavior [31–33].

The study of the SEI and the influence of the EDL is inherently challenging because it is controlled by a complex interplay of molecular-scale electrochemical formation and degradation processes that take place over hours, days, or even longer timescales. Most experimental methods that can achieve nanoscale resolution are limited to post-mortem and ex-situ analysis. Similarly, in-situ methods are typically limited in temporal or spatial resolution. This gap can be overcome by employing a combination of complex methods, but this is practically challenging [34].

Many computational modeling methods are employed to examine the dynamic behavior of SEI growth, but these also face challenges in scale and resolution [35–37]. Density functional theory (DFT) methods have been used to determine the complex reaction kinetics at the electrolyte/electrode interface [38], and Ab initio molecular dynamics has been employed to determine reaction mechanisms and interfacial behavior [39]. However, these methods are limited to studying a few hundred atoms at picosecond timescales, and thus are unable to capture the larger scale phenomena that guide SEI behavior. These scales are also too small to fully study the EDL, and they cannot include the influence of charging [40]. Classical molecular dynamics has been used to study electrolyte and ion solvation behavior [41], but is unable to capture the complex electrochemical reaction processes behind SEI formation and the EDL properties [42]. Continuum models are able to capture larger scale homogeneous phenomena over longer timescales and during charging, but are too coarse to observe the underlying heterogeneous atomistic- and molecular-scale phenomena [43–46].

Kinetic Monte Carlo (kMC) modeling is a promising alternative to overcome this discrepancy in scales, as it can provide molecular scale resolution of electrochemical phenomena at extended timescales [47]. Our group has previously employed kMC modeling and coupled kMC-continuum modeling to study SEI growth on lithium metal electrodes at open circuit [48], as well as on lithium ion batteries and SIBs during formation [25,49], including the impact of C-rate and electrolyte composition [47]. The kMC model presented in this work has been updated to include more precise electrochemical reactivity and ion migration, which enables a physically driven representation of the EDL. This lays the foundation for the unique analysis of many interfacial electrochemical applications, including batteries, electrocatalysts, and corrosion.

Herein, we perform rigorous DFT calculations to uncover novel reaction pathways of $NaPF_6$ decomposition and quantify their kinetics. These kinetic parameters are then used to power a kMC model of the hard carbon electrode/electrolyte interface with temporally and spatially dependent electrical potential. This study focuses on the role of NaF in the formation and properties of the SEI in SIBs. Additionally, the influence of charging rate, salt concentration, solvent ratio, and water contamination on the SEI and EDL are revealed.

2. Results and Discussion

2.1. Reaction Network and Kinetic Parameters

The DFT and kMC calculations in our prior work [25] revealed that the direct reductive decomposition of $NaPF_6$ is thermodynamically and kinetically unfavorable. Thus, the presence of NaF observed experimentally [18,19] suggests that $NaPF_6$ decomposition occurs via a more complex mechanism, such as reactions with water contamination [25]. In order to investigate other possible mechanisms of NaF generation, and to determine the kinetic parameters required for kMC simulations, DFT calculations were performed. We begin by analyzing the formation of NaF from $NaPF_6$ and Na^+. The reaction is started with the highly reversible reduction of $NaPF_6$ with a Na^+ ion at a standard electrochemical potential ($\Delta\Phi_0$) of -0.36 V vs. Na/Na^+, resulting in the formation of Na_2PF_6.

$$NaPF_6 + Na^+ + e^- \leftrightarrow Na_2PF_6 \quad (1a)$$

The further reaction of Na_2PF_6 to form $NaPF_5$ and NaF (Eq. 1b)

$$Na_2PF_6 \leftrightarrow NaPF_5 + NaF \quad (1b)$$

has an activation barrier of 17.71 kcal/mol and a reaction energy of 2.79 kcal/mol, and is thus kinetically and thermodynamically unfavorable. Therefore, we then explored the effect of additional Na^+ addition to the complex. We found that a more intricate mechanism occurs; Na_2PF_6 coordinates with an additional Na^+ and reorganizes to form a NaF-containing complex $NaPF_5NaFNa^+$ (Eq. 1c, Fig. S1a),

$$Na_2PF_6 + Na^+ \leftrightarrow NaPF_5NaFNa^+ \quad (1c)$$

with a reaction energy of -2.01 kcal/mol and a relatively low activation energy barrier of 5.26 kcal/mol. That is, further decomposition is possible when a NaF forms and remains complexed with the parent salt molecule.

This complex then undergoes a very favorable second reduction at a potential below 3.21 V vs. Na/Na^+ to form PF_3 and two additional NaF molecules (Eq. 1d),

$$NaPF_5NaFNa^+ + e^- \leftrightarrow PF_3 + 3NaF \quad (1d)$$

with a reaction free energy of -19.05 kcal/mol and an activation barrier of 7.76 kcal/mol. It is interesting to note that the three NaF produced in this reaction remain in a cluster (Fig. S1b), and could establish a possible site for additional nucleation.

These findings suggest that the overall self-catalyzed reductive decomposition of $NaPF_6$ to form PF_3 and NaF formation is kinetically and thermodynamically favorable.

We then investigated the influence of water contamination on $NaPF_6$ reactivity by placing an H_2O molecule near the salt. In addition to the implicit solvation field, one molecule each of both ethylene carbonate (EC) and propylene carbonate (PC) were explicitly included in order to

better represent for the local solvation environment around $NaPF_6$. The reaction initiates with the reduction of $NaPF_6$ and a Na^+ ion below a standard electrochemical potential ($\Delta\Phi_0$) of -0.72 V vs. Na/Na^+ (Eq. 2a).

$$NaPF_6 + Na^+ + e^- \overset{H_2O}{\longleftrightarrow} Na_2PF_6 \quad (2a)$$

This is followed by the formation of $NaPF_5$ and NaF, with a reaction free energy of -8.2 kcal/mol and an activation energy barrier of 7.19 kcal/mol (Eq. 2b).

$$Na_2PF_6 \overset{H_2O}{\longleftrightarrow} NaPF_5 + NaF \quad (2b)$$

Subsequently, $NaPF_5$ undergoes a second reduction with another Na^+ ion below a potential $\Delta\Phi_0$ of 2.19 V vs. Na/Na^+. Then, the process is followed by the formation of PF_3 and two NaF molecules, with a reaction free energy of 0.94 kcal/mol and an activation barrier of 14.09 kcal/mol (Eq. 2c).

$$NaPF_5 + Na^+ + e^- \overset{H_2O}{\longleftrightarrow} PF_3 + 2NaF \quad (2c)$$

The high potential barrier of step 2a, as well as the high activation and positive reaction energy of step 2c, indicate that the H_2O-catalyzed reductive decomposition of $NaPF_6$ is unfavorable. The direct hydrolysis of PF_5 was also investigated (Fig. S4) and was shown to be significantly unfavorable. Overall, these findings indicate that the H_2O-based decomposition of $NaPF_6$ is kinetically unfavorable, which is in agreement with recent experimental work [50].

The DFT results reveal that the self-catalyzed decomposition of $NaPF_6$ leading to NaF formation is both kinetically and thermodynamically favored, emerging as the dominant mechanism. In contrast, the contribution of water-based pathway is minimal due to higher activation barriers. These results serve as the foundational input for constructing a chemically realistic kMC model that captures the competing interfacial reaction pathways. In particular, the dominance of the self-catalyzed NaF formation pathway, as revealed by DFT, is reflected in the reaction network formulation.

These mechanistic insights from DFT calculations were subsequently combined with an EC and PC reduction reaction network established in prior work [25]. The overall network consists of EC and PC degradation to form Na_2CO_3 as well as the pathway to form the organic glycolate species. Several dimerization reactions are also included. Additionally, both the self-catalyzed and water-catalyzed pathways of $NaPF_6$ decomposition to form PF_3 and NaF are included. The overall reactions are detailed below:

$$NaPF_6 + 2Na^+ + 2e^- \leftrightarrow PF_3 + 3NaF \quad (1)$$

$$NaPF_6 + 2Na^+ + 2e^- \overset{H_2O}{\longleftrightarrow} PF_3 + 3NaF \quad (2)$$

$$EC + 2Na^+ + 2e^- \leftrightarrow Na_2CO_3 + C_2H_4 \quad (3)$$

$$EC + 2Na^+ + 2e^- \leftrightarrow NaO(CH_2)_2ONa + CO \quad (4)$$

$$PC + 2Na^+ + 2e^- \leftrightarrow Na_2CO_3 + CH_2CHCH_3 \quad (5)$$

$$PC + 2Na^+ + 2e^- \leftrightarrow NaOCH_2CH(CH_3)ONa + CO \quad (6)$$

$$2EC + 2Na^+ + 2e^- \leftrightarrow NaCO_3(CH_2)_2CO_3Na + C_2H_4 \quad (7)$$

$$EC + PC + 2Na^+ + 2e^- \leftrightarrow NaCO_3(CH_2)_2CO_3Na + CH_2CHCH_3 \quad (8)$$

$$EC + PC + 2Na^+ + 2e^- \leftrightarrow NaCO_3CH_2CH(CH_3)CO_3Na + C_2H_4 \quad (9)$$

$$2PC + 2Na^+ + 2e^- \leftrightarrow NaCO_3CH_2CH(CH_3)CO_3Na + CH_2CHCH_3 \quad (10)$$

These reactions consist of many intermediate steps that are outlined in detail in Table S1. The intermediate steps are implemented in the kMC model, but are not detailed here in order to improve clarity.

2.2. SEI Evolution

We incorporated the reaction network and kinetic parameters into the kMC framework and modeled the time-resolved evolution of the SEI over hard carbon during the first charge. The first system studied, defined as the 'Baseline', consisted of a 1:1 EC:PC mass ratio / 1M $NaPF_6$ electrolyte with 500ppm water contamination and a charging rate of 0.25. The relatively high H_2O concentration was chosen as a starting point to explore $NaPF_6$ reactivity. The initial stages of SEI growth consisted primarily of solvent decomposition to form Na_2CO_3. For lower electrical potentials, NaF formation became the dominant process, leading to the formation of a thin inner layer of Na_2CO_3 and thicker outer layer of NaF, as shown in Figure 1. All NaF was generated from the autocatalytic pathway (Eq. 1); formation via the water-catalyzed pathway (Eq. 2) did not occur at all in the simulations.

The SEI is significantly porous, with an average fractional occupancy of solid species of ~0.75 in the Na_2CO_3 layer and ~0.8 in the NaF layer. This porosity leads to increased electron leakage and will likely also contribute to mechanical instability. There is also a notable minimum of ~0.7 in the fractional occupancy at the Na_2CO_3/NaF interface, indicating poor adhesion, visible at the NaF/Na_2CO_3 interface in Figure 1, and an additional source of possible mechanical instability [51–53].

The porosity of the Na_2CO_3 layer and the minimum at the NaF-Na_2CO_3 interface is primarily due to the shift to NaF formation; as soon as the local potential becomes low enough to make NaF formation electrochemically favorable, available electrons preferentially reduce $NaPF_6$ rather than the solvent molecules near the surface. The close proximity of the NaF produced by the autocatalytic reaction leads to self-agglomeration and a lower diffusive driving force toward the Na_2CO_3, which is responsible for the higher porosity and reduced adhesion at the interface between the Na_2CO_3 and NaF layers.

The underlying mechanism of the continued porosity throughout the SEI is the electrostatic potential gradient within the EDL, which is visible in the net ionic charge of each layer, shown in the pink lines of Figure 1. The strong separation of Na^+ and PF_6^- at these layers impedes their coordination to form $NaPF_6$, which prevents Reaction 1 from occurring inside the SEI. Excess electrons instead travel to decompose $NaPF_6$ at or above the SEI surface, leading to SEI growth, which raises the height of the EDL, and the process repeats.

The thin and thus poorly-insulating SEI at the beginning of formation more readily leaks electrons, which causes an increased electrostatic potential gradient at the SEI/electrolyte interface, shown in the yellow lines of Figure 1. This increased potential gradient induces a more pronounced EDL, which contributes to the increased porosity at lower layers. As the SEI becomes thicker, the potential gradient decreases, leading to a less pronounced EDL and enabling the growth of a less porous SEI.

This system establishes a baseline for comparison to other systems with modified operating conditions, enabling the determination of the underlying mechanisms behind the various SEI properties and behavior observed in literature and informing the design of more robust SIBs.

2.2.1. Impact of System Design and Operating Conditions

We then investigated how NaF formation, SEI properties, and the EDL are influenced by system conditions. Specifically, we investigate the influence of water contamination, solvent ratio, salt concentration, and charging rate. These parameters are chosen because they have been suggested to influence the properties of the SEI and are relatively simple to modify experimentally. The specific systems and conditions are listed in Table 1. Consistent results were observed for simulations of the same systems with different random seeds, and are included in the SI (Fig S13-16).

Across all system conditions, only trace (less than 1%) amounts of organic species are formed, which is in agreement with prior work [25]. This is because the reduction of the solvent molecules to form Na_2CO_3 (Eq. 3 & 5) is more favorable than the pathway to form the glycolate

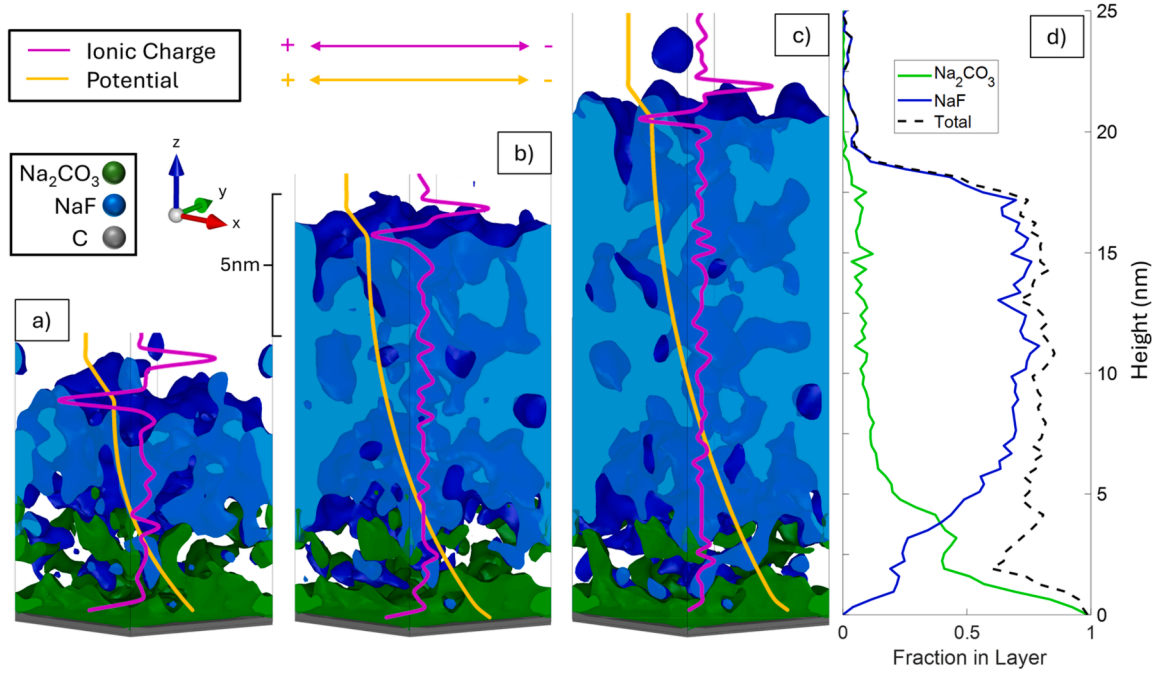

Figure 1. SEI growth during charging of HC electrode (baseline system, 1:1 EC:PC, 1M $NaPF_6$, 500ppm H_2O, 0.25C) at a) 10% SOC, b) 50% SOC, and c) 100% SOC. d) Fractional composition of each SEI layer in the kMC box at 100% SOC. Pink and yellow lines correspond to the qualitative behaviors of the net ionic charge (e) and electrical potential (V) of a given z-layer, respectively. Green and blue lines correspond the fraction of Na_2CO_3 and NaF, the dashed line is the total solid fraction.

Table 1
Varied formulations of the $NaPF_6$ EC:PC electrolyte systems over hard carbon studied with the kMC model. System names are based on the altered properties of the given system, i.e. $M_{.5}$ has a 0.5M salt concentration, and C_1M_1, has a C-rate of 1 and a 1M salt concentration. The baseline can also be described as $C_{.25}M_1$.

System	C-rate	EC:PC Mass Ratio	Salt Conc. (M)	ppm H_2O
Baseline	0.25	1:1	1	500
$M_{.5}$	0.25	1:1	0.5	500
M_2	0.25	1:1	2	500
M_3	0.25	1:1	3	500
C_1M_1	1	1:1	1	500
C_1M_2	1	1:1	2	500
$C_{.5}M_{.5}$	0.5	1:1	0.5	500
$C_{.5}M_1$	0.5	1:1	1	500
$C_{.5}M_2$	0.5	1:1	2	500
$So_{.25}$	0.25	1:4	1	500
So_4	0.25	4:1	1	500
W_{1k}	0.25	1:1	1	1000
$W_{2.5k}$	0.25	1:1	1	2500

species (Eq. 4 & 6, Table S1). The formation of dimer species (Eq. 7-10) is similarly unlikely due to the low availability of the necessary intermediate reactants ECNa or PCNa (Eq. 7a).

$$2ECNa \rightarrow NaCO_3(CH_2)_2CO_3Na + C_2H_4 \quad (7a)$$

The low availability of these intermediate species is due to the high reversibility of their formation reactions (Eq 3a & 5a), and the low barrier for their further reduction to form Na_2CO_3 (Eq 3b & 5b).

$$EC + Na^+ + e^- \leftrightarrow ECNa \quad (3a)$$

$$PC + Na^+ + e^- \leftrightarrow PCNa \quad (5a)$$

$$ECNa + Na^+ + e^- \leftrightarrow Na_2CO_3 + C_2H_4 \quad (3b)$$

$$PCNa + Na^+ + e^- \leftrightarrow Na_2CO_3 + CH_2CHCH_3 \quad (5b)$$

Because of the relatively high concentration of Na^+ (~0.24mol/L) [54], it is much more likely for ECNa to encounter a Na^+ than another ECNa (or PCNa), which only exist in mmol/L concentrations. Even if two ECNa do encounter each other, the relatively low reduction potential and reaction energy (-0.46V, -8.66 kcal/mol, Table S1) for the reverse of Reaction 3a means it is much more likely for one ECNa to oxidize back to EC, producing a Na^+ that can then react with the second ECNa (Eq. 3b). All of this indicates that the organic species observed experimentally are likely to form via a more complex mechanism, such as surface-catalyzed reactions, or via a HF cycle [55].

A further common outcome for all investigated conditions is that an inner layer of Na_2CO_3 is formed initially, followed by an outer layer of NaF. This occurs because the reduction potential for Na_2CO_3 formation is higher, allowing it to react more favorably. As the SEI becomes thicker and more insulating, the local electrical potential becomes lower, which increases the decomposition rate of $NaPF_6$ and triggers a dramatic shift in the composition of the SEI. We can conclude that without additional additives, EC/PC/ electrolyte systems will yield a porous layered system of a thin Na_2CO_3 layer followed by a broader NaF layer. The high porosity, as well as the significant presence of Na_2CO_3, is suboptimal; electrolyte composition and operating conditions should be modified in order to reduce porosity and increase NaF content. In the following, we elucidate the impact of salt, solvent and water concentration and C-rate on the forming SEI, respectively, to see possible handles to tailor SEI growth.

2.2.2. *Water Content and Solvent Ratio*

We studied systems with 2x and 5x higher water contamination (W_1, 1000ppm and W_2, 2500ppm) in order to further investigate its potential catalytic influence on SEI properties and determine if the absence of the water-catalyzed mechanism (Eq. 2) in the baseline scenario (500ppm H_2O) was only due to an insufficient presence of H_2O. Lower H_2O concentrations were not explored since there was no reactivity at 500ppm.

The water-catalyzed reaction also did not occur in either of the systems with elevated water content, further confirming that the pathway is limited by kinetic and thermodynamic barriers, rather than reactant availability. This is consistent with recent experimental findings, which observed minimal $NaPF_6$ decomposition even with direct

addition of H_2O over very long timescales, or when heating the systems [50,55]. We expect that observations of HF that have been reported experimentally elsewhere Because of this, both systems exhibited similar behavior to the baseline system in terms of SEI thickness, coulombic efficiency, and NaF content (Figure 2a-c). Higher amounts of $NaPF_6$ hydrolysis have been reported in cells with FEC and Na-metal electrodes, indicating that these may play a substantial role in the hydrolysis process, and should be investigated further [56].

We varied the mass ratio of EC and PC in the solvent ($So_{.25}$ 1:4 and So_4 4:1), including their corresponding dielectric constants (baseline scenario = 1:1), in order to understand the cause of the different behaviors observed experimentally [28,29]. Our prior work [25] determined that varied solvent ratios had minimal effect on SEI properties, but the novel incorporation of the EDL into the kMC model here may reveal that they influence the system by modifying EDL behavior via their different dielectric constants.

The systems with varied solvent ratio, $So_{.25}$ and So_4, also formed SEIs similar to the baseline. There were only minimal differences in Coulombic efficiency and SEI thickness (Fig. 2a,c) and in the SEI porosity and structure of the EDL (Fig. S6). So_4, the system with a 4:1 EC:PC mass ratio, had a minor decrease of ~3% of NaF content in the SEI (Fig. 2b). These minor differences are in contrast to the large difference in the amount of each solvent consumed (Figure 2d) and in the dielectric constants, 67.9 for $So_{.25}$ and 86.4 for So_4. Within the scope of the current kMC model, these results suggest that variations in solvent ratio and dielectric constant alone do not fully account for the improved behavior observed in literature [28] for higher PC contents. Instead, more complex effects, such as changes in ion solvation phenomena, may contribute to the observed behavior. Further investigation of the ion solvation shell is therefore needed [56].

2.2.3. Salt Concentration

Since the self-catalyzed mechanism was determined to be the driving mechanism for NaF growth in the SEI, the next set of simulations focused on determining the influence of the conductive salt concentration on SEI formation. The results for systems with a C-rate of 0.25, water content of 500ppm, EC:PC ratio of 1:1, and 0.5 M, 2 M, and 3 M $NaPF_6$ ($M_{0.5}$, M_2, M_3) are shown in comparison with the baseline system in Figure 3.

Systems with higher salt concentrations exhibited higher coulombic efficiency and formed thinner SEIs with higher NaF content (Fig. 3a,b). However, this effect is diminished when the concentration becomes very high, as indicated in Figure 3a, where the efficiency of the systems with 2 and 3 molar salt concentrations are almost identical. This is also illustrated in the trend of SEI thickness, where the SEI thickness and rate of growth is similar for the two systems at 100% SOC. The SEI exhibits an increasing fractional occupation of solid species, and thus a decrease in porosity, with increasing salt content, shown in Figure 3b, which corresponds to improved passivation and mechanical stability. This effect is inhibited at higher salt concentrations, where the formation of clusters at the surface leads to a lower density. This finding corresponds with literature results [27], and its implications will be further explored in the next section (2.2.4) in combination with charging rate variation.

The predominant SEI formation mechanism for all systems in this study is via reaction at the surface, leading to layer-by-layer growth. However, for some systems, additional growth occurs via secondary particle nucleation in the electrolyte. This effect is most pronounced for the 3 molar salt concentration (Figure 3c). This particle growth occurs due to the higher salt concentration leading to a higher formation rate of NaF, which catalyzes further NaF formation, lowering the barrier for salt decomposition in solution, away from the interface. This additional SEI growth mechanism is one of the primary reasons for the diminishing benefits shown in Figure 3a and 3b, and also likely contributes to the worsened behavior observed experimentally at high concentrations and charge rates, which will be explored further in the next section (2.2.4) [27]. This detrimental growth mechanism could possibly be mitigated by controlling the nucleation behavior of the system [57,58], and should be investigated further in future studies.

2.2.4. Interaction of Salt Concentration and Charging Rate

The formation of the SEI was studied under different C-rates and with varied salt concentrations in order to better understand how their interplay influences SEI properties [27]. The results are shown in

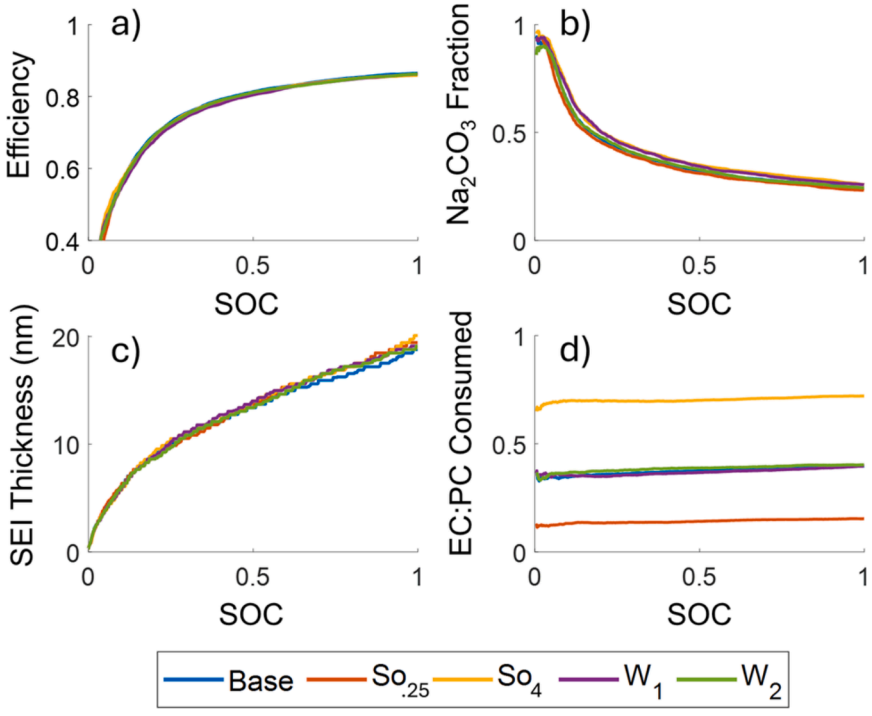

Figure 2. SEI evolution and properties during first charge at 0.25 C in systems with varied solvent ratios ($So_{.25}$ 1:4 and So_4 4:1) and amounts of water contamination (W_1, 1000ppm and W_2, 2500ppm, details in Table 1). a) Efficiency, b) molar fraction of Na_2CO_3 in the SEI, c) SEI thickness, and d) EC:PC consumed.

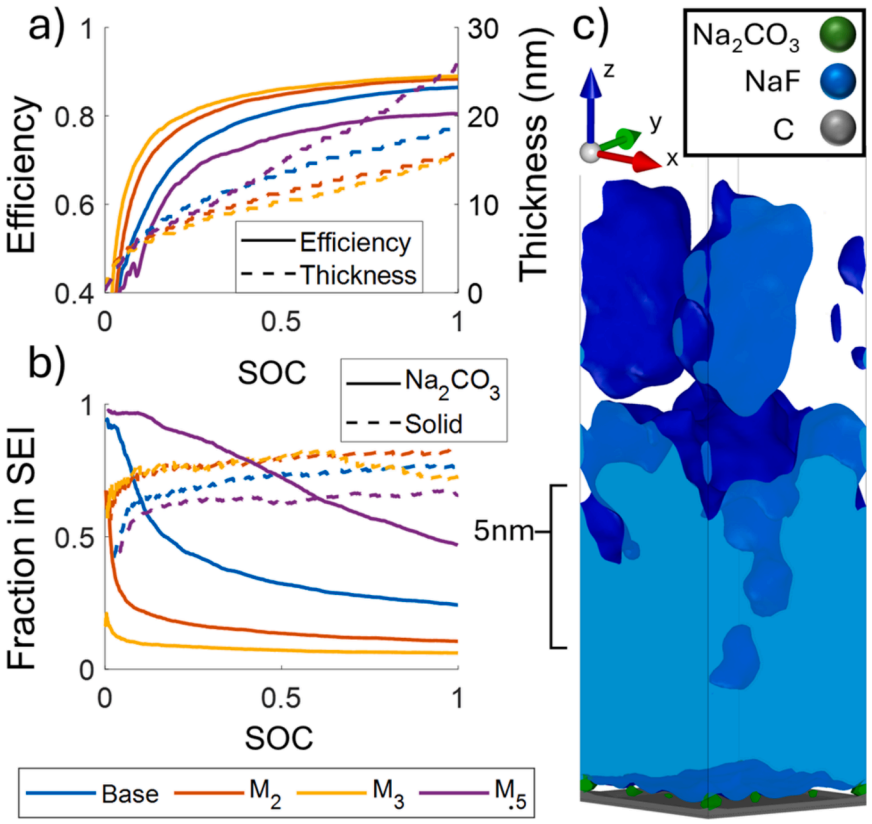

Figure 3. SEI evolution and properties during first charge at 0.25C in systems in systems with varied $NaPF_6$ concentration. a) Coulombic efficiency and SEI thickness, b) Fraction of Na_2CO_3 and solid species in SEI, for systems with varied salt concentration. c) The SEI formed at 100% SOC in the 3 molar $NaPF_6$ system. Subscripts correspond to molar concentration of $NaPF_6$ in the electrolyte. Additional system information is available in Table 1. Solvent, salt, and intermediate species are removed for ease of visualization.

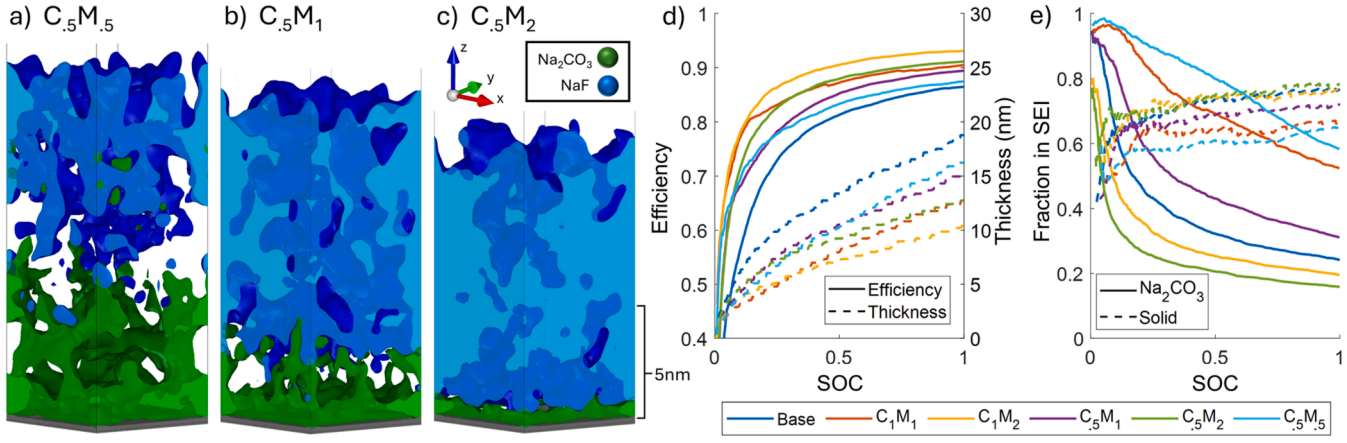

Figure 4. SEI properties in systems with varied C-rate and salt concentration. a-c) morphology of the SEIs formed in systems $C_{.5}M_{.5}$, $C_{.5}M_1$, $C_{.5}M_2$. Na_2CO_3 is shown in green and NaF in blue. Solvent, salt, and intermediate species are removed for ease of visualization. d) Coulombic efficiency and SEI thickness. e) Fraction of Na_2CO_3 and solid species in the SEI. C subscripts correspond to the C-rate, and M subscripts correspond to the molar concentration of $NaPF_6$ in the electrolyte. Additional system information is available in Table 1.

Figure 4.

Systems with an elevated C-rate of 1, C_1M_1 and C_1M_2, exhibited the thinnest SEIs and highest first cycle coulombic efficiency. The systems with a C-rate of 0.5, $C_{.5}M_{.5}$, $C_{.5}M_1$, and $C_{.5}M_2$, were less efficient than their corresponding 1C systems, but more efficient than the 0.25C baseline, establishing a clear trend of improved performance with higher C-rate (Figs. 4d, S7, and S8). Higher C-rates also correlated to how quickly the SEI was formed and approached a stable state, as evidenced by the leftward shift of the efficiency curves in Figures 4d and S9. This is because higher C-rates generate a more rapid drop in potential and increase the porosity of the SEI, which induces a higher rate of Na^+ migration to the electrode surface where it can be intercalated. The SEI exhibited a decrease in the relative amount of NaF and increased porosity (decreased solid fraction) with increasing C-rate (Figure 4e), which corresponds to reduced passivation and lower mechanical stability, and thus likely contributes to decreased long-term stability of the

cell.

Low salt concentrations had the worst performance for each of the charging rates tested. System $C_{.5}M_{.5}$ outperforms the baseline ($C_{.25}M_1$) initially, but the rate of SEI growth remains relatively constant, and the rate of efficiency increase begins to slow down. This leads to a relatively constant ratio between Na^+ consumed for SEI formation vs. intercalation, indicating that the SEI is far from being stabilized and will continue to grow. This instability is further exemplified in the highly porous and nonuniform SEI shown in Figure 4a. We attempted to simulate a system with 0.5 M $NaPF_6$ at 1C, but the calculations quickly became unstable because the low availability of cations for charge transfer led to huge spikes in local potential and rapid system instability. This is the first theoretical explanation of the probable underlying mechanism of experimentally observed behavior where increased C-rates with low salt concentrations lead to battery failure [27].

The influence of salt concentration established in the previous section (2.2.3) for 0.25C systems was confirmed for different C-rates here, where for a given charging rate, systems with higher concentrations of the conductive salt $NaPF_6$ in the electrolyte also exhibited higher efficiency and thinner SEIs. However, this improved behavior occurs via a different mechanism compared to what occurs with increased C-rates. This is visible in the behavior of the systems with a C-rate of 0.5 in Figures 4d and S9a, where the higher salt concentration in $C_{.5}M_2$ leads to a significantly lower rate of SEI growth by the end of the first charge compared to $C_{.5}M_1$. This improved stability is due to the higher content of NaF and lower porosity in the SEI, which leads to lower electron leakage and reduced reactivity. This corresponds to increased long-term stability, which is also evidenced in the upward shift of the efficiency curves in Figures 4d and S9a. The diminishing returns to the effect of increased salt concentration observed in the previous section (2.2.3) are also further evidenced at higher C-rates, as shown by Figures 4d and S8, where the rate of change in SEI thickness, Coulombic efficiency, and NaF concentration between the 0.5M and 1M systems is significantly higher than between the 1M and 2M systems.

These effects are further revealed in the changes to the porosity and thickness of the SEI, as shown in Figures 4a-c and S7. It is clear that C-rate has a stronger effect on SEI thickness and increasing porosity, and salt concentration has a larger effect on NaF content and decreasing porosity. The cause of the increased porosity in these systems is the same as discussed previously; higher C-rates lead to higher potential gradients, which leads to a more pronounced EDL, which then impedes the formation of a uniform SEI. The excess salt in the high-concentration systems overcomes this issue by simply providing more opportunities for association to form $NaPF_6$ and subsequent decomposition.

High C-rates can offset the efficiency loss of low salt concentrations and, similarly, high salt concentrations can offset the loss from low C-rates, as evidenced by the similar efficiency and SEI thickness of systems $C_{.5}M_2$, and C_1M_1 in Figure 4d. Higher salt concentrations can also negate the increased porosity and decreased NaF content in the SEI from high C-rates. These findings indicate that an optimum can be found between high C-rate and high salt concentration that minimizes SEI thickness and formation time (first cycle efficiency) while maximizing NaF content and SEI density (long term stability).

2.2.5. *The Electrical Double Layer*

Prior studies have speculated on the influence of the EDL on the SEI, but until now, models have not been able to clearly grasp its effect at this resolution and scale [59–61]. The novel implementation of ion migration based on the coupling of spatially and temporally dependent electronic and coulombic potentials in our model allows for the electrostatic potential gradient of the EDL to be approximated at the molecular scale during charging. The previous sections have revealed that properties of the EDL play a significant, but complex role in the behavior of the SEI. In this section, we seek to better understand this relationship.

The EDL is clearly visible in the ionic charge distribution (number of Na^+ - number of PF_6^-) at 100% SOC in the selected systems in Figure 5. Figure 5 also displays the morphology of the SEI on each z-layer. It is interesting to note that the cluster nucleation in the electrolyte in system M_3 discussed in the prior section (2.2.3) and Figure 3c is also visible in Figure 5g. It is also notable that the EDL in this system resides in a z-layer near the middle of the cluster instead of above it or at the SEI surface. This is because the cluster is not sufficiently electronically insulating to create an electronic potential driving force to push the EDL to its top surface, but it does partially block ion transport to the surface, which creates an electrostatic driving force to pull the EDL away from the SEI surface.

The EDL was significantly influenced by salt concentration and C-rate, with salt concentration having a larger effect. Higher C-rates and

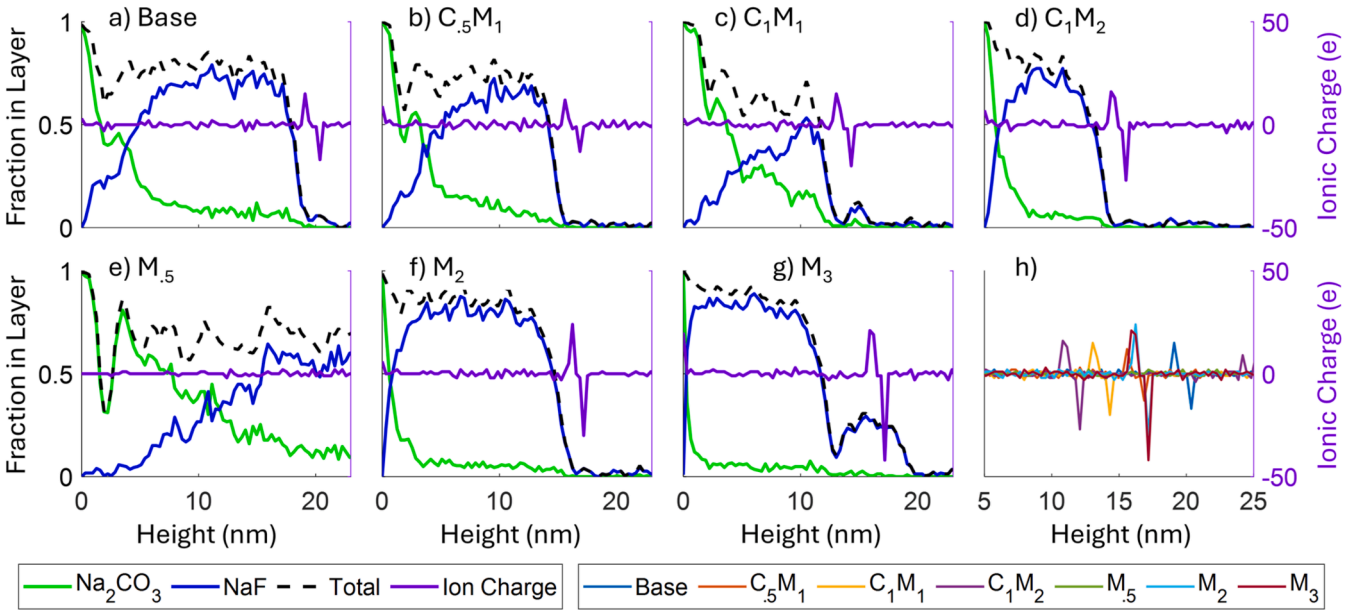

Figure 5. Visualization of EDL and SEI composition over HC surface at 100% SOC after first charge for selected systems. a-g) Fractional SEI composition and ionic charge (number of Na^+ - number of PF_6^-) of vs height. h) The ionic charges of all systems overlayed together. C subscripts correspond to C-rate, and M subscripts correspond to molar $NaPF_6$ concentration in the electrolyte. Further system details are available in Table 1.

higher salt concentrations both caused the formation of a stronger and more pronounced EDL (Figure 5c,d,f,g), and lower C-rates and salt concentrations corresponded to a smaller and more diffuse layer (Figure 5a,e).

Increased C-rate only has a moderate effect on the EDL at 100% SOC, as evidenced by the relatively small differences between the Baseline ($C_{.25}M_1$), $C_{.5}M_1$, and C_1M_1 (Figure 5a-c). This is not the case for salt concentration, where there is a notable increase in the magnitude of the EDL for each increase in concentration (Figure 5a,e-g).

This influence of C-rate is more pronounced at the beginning of charge, when the SEI is thin and poorly insulating, as visible in Figure S10. The increased magnitude of the EDL here is due to the increased current creating an increased electrical potential gradient at the interface, which leads to a stronger electrical field acting on the ions. The phenomenon is the reason for the higher porosity in the lower regions of the SEI. As the SEI becomes thicker, this effect is reduced (Figure S11) which allows the SEI to grow more uniformly.

The increased magnitude of the EDL in systems with higher salt concentration is primarily due to the increased availability of ions, and not to the potential gradient. In fact, higher salt concentrations served to lessen the potential gradient at the interface at low SOC by generating a more insulating SEI, as visible in Figure S10 [a vs. f], [b vs. g], and [c vs. h]. These findings provide insight on how C-rate and salt concentration could be carefully controlled during formation in order to direct EDL behavior and, by extension, SEI properties [62]. Formation protocols should consist of low C-rates at low SOCs, followed by increased C-rates starting at medium SOCs.

The increased magnitude of the EDL caused by the higher C-rates and salt concentrations directly influences the reactivity changes observed in the prior sections, but is also likely to impact more complex phenomena, such as ion desolvation and solvation sheath structure, that are not yet fully captured in our model. Future work should aim to investigate the precise effect of the magnitude of the EDL in these processes [63].

3. Conclusion

In this work, we have employed first principles calculations to determine novel decomposition mechanisms for $NaPF_6$ during formation in SIBs, as well as their corresponding kinetic parameters. These findings revealed that a self-catalytic reduction involving NaF is the dominant mechanism, and that the hydrolysis of $NaPF_6$ is kinetically unfavorable. These parameters were then incorporated into a kMC model of SEI growth during first charge.

The kMC simulations reveal SEIs that consist of an inner Na_2CO_3 layer and an outer NaF layer, with varied ratios, depending on electrolyte compositions and C-rate. Water contamination was found not to have any impact. The altered dielectric constant of systems with different solvent ratios has a minimal effect on the EDL and properties of the SEI. High C-rates rapidly form thinner SEIs with higher coulombic efficiencies (due to more rapid passivation), but with higher Na_2CO_3 content and increased porosity, which are likely to exhibit reduced long-term stability compared to dense SEIs with high NaF content. Higher salt concentrations generate thinner, denser, and more efficient SEIs, with higher fractions of NaF, but provide diminishing returns when concentration is increased above 2M. An important relationship between salt concentration and C-rate and their effect on the SEI was established: Low salt concentrations were shown to be incompatible with high C-rates due to low Na^+ availability, which caused large spikes in local electrical potential, leading to uncontrolled reactivity and cell failure. These findings indicate that a balance of C-rate and $NaPF_6$ concentration can be found that minimizes SEI porosity and maximizes NaF content (long-term stability) while minimizing SEI thickness and stabilization time (first cycle efficiency).

The influence of the EDL potential gradient was approximated at the molecular scale during charge, and was determined to be the underlying cause of the varied SEI properties associated with different C-rates and salt concentrations. This is primarily due to the ability of the EDL to control the supply of ionic salt species made available for reaction at the electrode surface. The larger electrostatic potential gradients induced by higher C-rates cause an increase in the magnitude of the EDL, which leads to an increase in SEI porosity by limiting ion supply to the surface. This effect is diminished at high SOCs after the SEI becomes sufficiently insulating. Increased salt concentrations decrease SEI porosity by providing enough excess ions to distribute the electrostatic potential and facilitate transport to the surface. However, when salt concentration becomes too high, the EDL cannot sufficiently mediate excess ion supply to the surface, leading to increased reactivity and SEI growth. These findings can be used to direct the tuning of C-rate and salt concentration during formation in order to control EDL behavior and SEI properties. We suggest formation protocols consisting of low C-rates at low SOCs, then switching to higher C-rates at medium SOCs, in combination with a 1-2M $NaPF_6$ concentration.

Overall, this work clarifies the effect of the complex relationship between C-rate, salt concentration, and system properties on the structure of the EDL and the composition of the SEI. The novel kMC model developed here establishes the groundwork for the future study of the role of the EDL in many electrochemical applications, including varied battery chemistries, electrocatalysis, and corrosion.

CRediT authorship contribution statement

Kie Hankins: Writing – review & editing, Writing – original draft, Visualization, Validation, Resources, Methodology, Investigation, Formal analysis, Data curation, Conceptualization. **Miftahussurur Hamidi Putra:** Writing – review & editing, Writing – original draft, Visualization, Validation, Investigation, Formal analysis, Data curation. **Axel Gross:** Writing – review & editing, Supervision, Resources, Project administration, Funding acquisition. **Ulrike Krewer:** Writing – review & editing, Supervision, Project administration, Funding acquisition, Conceptualization.

Declaration of competing interest

The authors declare that they have no known competing financial interests or personal relationships that could have appeared to influence the work reported in this paper.

Acknowledgements

This work was funded by the German Research Foundation (DFG) under Project ID 390874152 (POLiS Cluster of Excellence). M.H.P. and A.G. thank the DFG for financial support through Project C5 of the Transregional Collaborative Research Centre TRR234 CataLight (Project No.364549901). The authors gratefully acknowledge support by the state of Baden–Württemberg through bwHPC and the German Research Foundation (DFG) through grant no INST 40/575-1 FUGG (JUSTUS 2 cluster).

Supplementary materials

Supplementary material associated with this article can be found, in the online version, at doi:10.1016/j.ensm.2026.105392.

Data availability

Data Repository link is included in manuscript. Data cannot be removed or edited after it is uploaded, so we will upload it after final review is complete in order to ensure completeness.

References

[1] H.S. Hirsh, Y. Li, D.H.S. Tan, M. Zhang, E. Zhao, Y.S. Meng, Adv. Energy Mater. 10 (2020) 2001274.
[2] L.J. Hounjet, Energy Storage 4 (2022) e309.
[3] A. Rudola, R. Sayers, C.J. Wright, J. Barker, Nat. Energy 8 (2023) 215–218.
[4] R. Wanison, W.N.H. Syahputra, N. Kammuang-lue, P. Sakulchangsatjatai, C. Chaichana, V.U. Shankar, P. Suttakul, Y. Mona, J. Energy Storage 100 (2024) 113497.
[5] J. Peters, D. Buchholz, S. Passerini, M. Weil, Energy Environ. Sci. 9 (2016) 1744–1751.
[6] M. Baumann, M. Häringer, M. Schmidt, L. Schneider, J.F. Peters, W. Bauer, J. R. Binder, M. Weil, Adv. Energy Mater. 12 (2022) 2202636.
[7] C. Randall, First sodium-ion battery EVs go into serial production in China - electrive. com, https://www.electrive.com/2024/01/02/first-sodium-ion-battery-evs-go-into-serial-production-in-china/, (accessed 24 January 2025).
[8] L. Zhao, T. Zhang, W. Li, T. Li, L. Zhang, X. Zhang, Z. Wang, Engineering 24 (2023) 172–183.
[9] J. Lee, J. Kim, S. Kim, C. Jo, J. Lee, Mater. Adv. 1 (2020) 3143–3166.
[10] F. Baakes, D. Witt, U. Krewer, Chem. Sci. 14 (2023) 13783–13798.
[11] C. Yan, L.-L. Jiang, Y.-X. Yao, Y. Lu, J.-Q. Huang, Q. Zhang, Angew. Chem. 133 (2021) 8602–8606.
[12] M. Ma, H. Cai, C. Xu, R. Huang, S. Wang, H. Pan, Y.-S. Hu, Adv. Funct. Mater. 31 (2021) 2100278.
[13] S. Saleh, S. Daboss, T. Philipp, D. Schäfer, M. Rohnke, C. Kranz, ChemElectroChem 12 (2025) e202400707.
[14] Y.-X. Yao, J. Wan, N.-Y. Liang, C. Yan, R. Wen, Q. Zhang, J. Am. Chem. Soc. 145 (2023) 8001–8006.
[15] A. Marzouk, V. Ponce, L. Benitez, F.A. Soto, K. Hankins, J.M. Seminario, P. B. Balbuena, F. El-Mellouhi, J. Phys. Chem. C 122 (2018) 25858–25868.
[16] K. Palanisamy, S. Daboss, J. Romer, D. Schäfer, M. Rohnke, J.K. Flowers, S. Fuchs, H.S. Stein, M. Fichtner, C. Kranz, Batter. Supercaps 7 (2024) e202300482.
[17] J. Song, G. Jeong, A.-J. Lee, J.H. Park, H. Kim, Y.-J. Kim, ACS Appl. Mater. Interfaces 7 (2015) 27206–27214.
[18] J. Fondard, E. Irisarri, C. Courrèges, M.R. Palacin, A. Ponrouch, R. Dedryvère, J. Electrochem. Soc. 167 (2020) 070526.
[19] G.G. Eshetu, T. Diemant, M. Hekmatfar, S. Grugeon, R.J. Behm, S. Laruelle, M. Armand, S. Passerini, Nano Energy 55 (2019) 327–340.
[20] M. Dahbi, T. Nakano, N. Yabuuchi, S. Fujimura, K. Chihara, K. Kubota, J.-Y. Son, Y.-T. Cui, H. Oji, S. Komaba, ChemElectroChem 3 (2016) 1856–1867.
[21] R. Mogensen, D. Brandell, R. Younesi, ACS Energy Lett 1 (2016) 1173–1178.
[22] M. Fei, L. Qi, S. Han, Y. Li, H. Xi, Z. Lin, J. Wang, C. Ducati, M. Chhowalla, R. V. Kumar, Y. Jin, J. Zhu, Angew. Chem. Int. Ed. 63 (2024) e202409719.
[23] E. Wang, J. Wan, Y.-J. Guo, Q. Zhang, W.-H. He, C.-H. Zhang, W.-P. Chen, H.-J. Yan, D.-J. Xue, T. Fang, F. Wang, R. Wen, S. Xin, Y.-X. Yin, Y.-G. Guo, Angew. Chem. Int. Ed. 62 (2023) e202216354.
[24] E. Kohan, R. Khoshnavazi, M.Ghasem Hosseini, A. Salimi, M. Salami-Kalajahi, J. Mater. Chem. A 12 (2024) 30190–30248.
[25] K. Hankins, M.H. Putra, J. Wagner-Henke, A. Groß, U. Krewer, Adv. Energy Mater. (2024) 2401153.
[26] H. Wang, C. Zhu, J. Liu, S. Qi, M. Wu, J. Huang, D. Wu, J. Ma, Angew. Chem. 134 (2022) e202208506.
[27] C. Geng, D. Buchholz, G.-T. Kim, D.V. Carvalho, H. Zhang, L.G. Chagas, S. Passerini, Small Methods 3 (2019) 1800208.
[28] Y. Jin, P.M.L. Le, P. Gao, Y. Xu, B. Xiao, M.H. Engelhard, X. Cao, T.D. Vo, J. Hu, L. Zhong, B.E. Matthews, R. Yi, C. Wang, X. Li, J. Liu, J.-G. Zhang, Nat. Energy 7 (2022) 718–725.
[29] Z. Tian, Y. Zou, G. Liu, Y. Wang, J. Yin, J. Ming, H.N. Alshareef, Adv. Sci. 9 (2022) 2201207.
[30] L. Derr, M. Lang, K. Palanisamy, C. Kranz, R. Schuster, J. Phys. Chem. C 129 (2025) 4025–4031.
[31] Q. Wu, M.T. McDowell, Y. Qi, J. Am. Chem. Soc. 145 (2023) 2473–2484.
[32] J. Kim, F. Zhao, L.K.S. Bonagiri, Q. Ai, Y. Zhang, Chem. Mater. 36 (2024) 9156–9166.
[33] Z. Fan, W. Zhao, S. Shi, M. Zhou, J. Li, Y. Liu, Z. Pan, X. Yang, Angew. Chem. 137 (2025) e202416582.
[34] D. Schäfer, K. Hankins, M. Allion, U. Krewer, F. Karcher, L. Derr, R. Schuster, J. Maibach, S. Mück, D. Kramer, R. Mönig, F. Jeschull, S. Daboss, T. Philipp, G. Neusser, J. Romer, K. Palanisamy, C. Kranz, F. Buchner, R.J. Behm, A. Ahmadian, C. Kübel, I. Mohammad, A. Samoson, R. Witter, B. Smarsly, M. Rohnke, Adv. Energy Mater. (2024) 2302830.
[35] J. Wu, Chem. Rev. 122 (2022) 10821–10859.
[36] M. Becker, P. Loche, M. Rezaei, A. Wolde-Kidan, Y. Uematsu, R.R. Netz, D. J. Bonthuis, Chem. Rev. 124 (2024) 1–26.
[37] A. Bouibes, N. Takenaka, K. Kubota, S. Komaba, M. Nagaoka, RSC Adv 12 (2022) 971–984.
[38] E. Olsson, J. Cottom, H. Alptekin, H. Au, M. Crespo-Ribadeneyra, M.-M. Titirici, Q. Cai, Small 18 (2022) 2200177.
[39] K. Hankins, V. Prabhakaran, S. Wi, V. Shutthanandan, G.E. Johnson, S. Roy, H. Wang, Y. Shao, S. Thevuthasan, P.B. Balbuena, K.T. Mueller, V. Murugesan, J. Phys. Chem. Lett. 12 (2021) 9360–9367.
[40] S. Sakong, J. Huang, M. Eikerling, A. Groß, Curr. Opin. Electrochem. 33 (2022) 100953.
[41] X. Gao, J. You, L. Deng, B. Zhang, Y. Li, W. Wang, J. Mater. Chem. A 12 (2024) 25211–25221.
[42] L. Zeng, X. Ji, J. Zhang, N. Huang, Z. Wang, D. Yu, J. Peng, G. Feng, WIREs Comput. Mol. Sci. 15 (2025) e70009.
[43] F. Baakes, D. Witt, U. Krewer, Chem. Sci. 14 (2023) 13783–13798.
[44] H. Tao, S. Wang, H. Liu, C. Lian, Angew. Chem. Int. Ed. 64 (2025) e202418447.
[45] F. Single, A. Latz, B. Horstmann, ChemSusChem 11 (2018) 1950–1955.
[46] Y. Wang, H. Wang, G. Dang, X. Zhu, Q. Fu, Energy Fuels 39 (2025) 20908–20920.
[47] F. Röder, R.D. Braatz, U. Krewer, Comput. Chem. Eng. 121 (2019) 722–735.
[48] J. Wagner-Henke, D. Kuai, M. Gerasimov, F. Röder, P.B. Balbuena, U. Krewer, Nat. Commun. 14 (2023) 6823.
[49] F. Röder, R.D. Braatz, U. Krewer, J. Electrochem. Soc. 164 (2017) E3335–E3344.
[50] P.J. Buitrago Botero, A.W. Ells, A. Svirinovsky-Arbeli, M. Juelsholt, L.E. Marbella, J. Am. Chem. Soc. 147 (2025) 9159–9174.
[51] Y. Xu, H. Jia, P. Gao, D.E. Galvez-Aranda, S.P. Beltran, X. Cao, P.M.L. Le, J. Liu, M. H. Engelhard, S. Li, G. Ren, J.M. Seminario, P.B. Balbuena, J.-G. Zhang, W. Xu, C. Wang, Nat. Energy 8 (2023) 1345–1354.
[52] H. Adenusi, G.A. Chass, S. Passerini, K.V. Tian, G. Chen, Adv. Energy Mater. 13 (2023) 2203307.
[53] A. Bouibes, N. Sakaki, M. Nagaoka, ACS Omega 8 (2023) 16570–16578.
[54] D. Morales, L.G. Chagas, D. Paterno, S. Greenbaum, S. Passerini, S. Suarez, Electrochimica Acta 377 (2021) 138062.
[55] P. Barnes, K. Smith, R. Parrish, C. Jones, P. Skinner, E. Storch, Q. White, C. Deng, D. Karsann, M.L. Lau, J.J. Dumais, E.J. Dufek, H. Xiong, J. Power Sources 447 (2020) 227363.
[56] Y. Liu, R. Jiang, H. Xiang, Z. Huang, Y. Yu, Electrochimica Acta 425 (2022) 140746.
[57] Q. Li, Y. Zhang, X. Guo, Z. Yang, Y. Wang, Y. Chen, Y. Liu, H. Yue, S. Gao, H. Zhou, J. Huang, M. Shakouri, Y. Wang, G. Zhu, Z. Liu, Y. Zhang, H. Pang, Angew. Chem. Int. Ed. 64 (2025) e202509741.
[58] Q. Wang, Z. Zhang, Z. Hu, W. Du, Y. Zhang, M. Ye, Z. Wen, Y. Tang, X. Liu, C.C. Li, Angew. Chem. Int. Ed. 64 (2025) e202420772.
[59] R. Xu, X. Shen, X.-X. Ma, C. Yan, X.-Q. Zhang, X. Chen, J.-F. Ding, J.-Q. Huang, Angew. Chem. Int. Ed. 60 (2021) 4215–4220.
[60] J. Luo, K. Yang, J. Gai, X. Zhang, C. Peng, C. Qin, Y. Ding, Y. Yuan, Z. Xie, P. Yan, Y. Cao, J. Lu, W. Chen, Angew. Chem. Int. Ed. 64 (2025) e202419490.
[61] Q. Wu, M.T. McDowell, Y. Qi, J. Am. Chem. Soc. 145 (2023) 2473–2484.
[62] X. Yuan, D. Cheng, B. Liu, K. Liang, K. Liang, J. Yu, M. Mecklenburg, P. Sautet, Y. Li, Joule 8 (2024) 3038–3053.
[63] W. Yao, M.-H. Pai, A. Manthiram, Angew. Chem. 137 (2025) e202424547.